Combustion and Flame 283 (2026) 114549

Contents lists available at ScienceDirect

Combustion and Flame

journal homepage: www.sciencedirect.com/journal/combustion-and-flame

Thermoacoustic feedback mechanisms for premixed burners with a reacting hydrogen-methane jet in cross-flow

Philip Bonnaire [a,*], Sven Romeikat [a], Lukasz Panek [b], Oliver Lammel [c], Jonas Eigemann [d], Andreas Kempf [d], Wolfgang Polifke [a]

[a] Technical University of Munich, TUM School of Engineering and Design, Department of Engineering Physics and Computation, Boltzmannstr. 15, Garching, 85747, Germany
[b] Siemens Energy Global GmbH & Co. KG, Huttenstr. 12, Berlin, 10553, Germany
[c] German Aerospace Center (DLR), Institute of Combustion Technology, Pfaffenwaldring 38-40, Stuttgart, 70569, Germany
[d] University of Duisburg–Essen, Institute for Energy and Materials Processes (EMPI), Chair of Fluid Dynamics, Carl-Benz-Str. 199, Duisburg, 47057, Germany

ARTICLE INFO

Keywords:
Reacting jet in cross-flow
Hydrogen-methane fuel blend
Thermoacoustics

ABSTRACT

Understanding the interaction mechanisms between acoustic pressure pulsations and heat release of the flames is essential for preventing thermoacoustic instabilities in gas turbines. This study focuses on an industrial burner design under high-pressure operating conditions with a first and a second stage, the latter realized as a reacting jet in cross-flow. The premixed hydrogen-methane-air flames cause high-frequency instabilities of several thousand Hertz. The hydrodynamic structure of the reacting jet opens up new pathways for establishing feedback loops for instabilities. Large eddy simulations are performed for a technically premixed and a perfectly premixed second stage to evaluate the role of equivalence ratio fluctuations.

The technically premixed simulation demonstrates that the displacement of the flame front orthogonal to the jet axis, caused by the acoustic velocity of a longitudinal mode, can significantly affect the flame surface, producing delayed fluctuations in heat release that can amplify pressure oscillations in accordance with the Rayleigh criterion.

In the case of a perfectly premixed axial stage, the system exhibits a rotating transverse-longitudinal mixed mode. This mode modulates at much higher frequency and is accompanied by strong shear layer activity. Phasor diagrams demonstrate that the instability is driven by the compression of the cold gases. Surprisingly, flame surface modulations are out of phase with heat release fluctuations.

Those results demonstrate two distinct feedback mechanisms for high-frequency instabilities in staged combustion.

Novelty and significance statement

For the first time, this study investigates a technically and perfectly premixed reacting jet in cross-flow with hydrogen addition under self-excited thermoacoustic instabilities. A technically relevant configuration at elevated pressure (7 bar) is considered in numerical simulations as well as experiments. Due to the asymmetry of the jet trajectory, the jet can respond to orthogonal velocity perturbations relative to the jet axis at the same frequency. The mechanism triggered by these orthogonal velocity fluctuations amplifies in regions where the acoustic velocity is ahead of the pressure and thus depends on the chamber impedance. This criterion must be considered when placing the second stage. Furthermore, we show that in the absence of equivalence perturbations, the reacting transverse jet strongly responds to the density fluctuation of the transverse mode. Thus, the heat release perturbations are inevitably in phase with the pressure fluctuations.

1. Introduction

Gas turbines are reliable and flexible power suppliers that stabilize electrical grids when weather conditions do not allow the utilization of wind and solar energy. Operating gas turbines with hydrogen reduces their carbon emissions and makes them an essential technology on the way to a carbon-neutral future. Sequential combustors, which inject a portion of the fuel at a downstream location of the chamber, e.g., by a reacting jet in cross-flow (RJC), gain interest due to their capability

* Correspondence to: Technical University of Munich, Boltzmannstr. 15, Garching, 85747, Germany.
E-mail address: philip.bonnaire@tum.de (P. Bonnaire).

https://doi.org/10.1016/j.combustflame.2025.114549
Received 5 June 2025; Received in revised form 13 October 2025; Accepted 14 October 2025
Available online 24 October 2025

to further increase the operational flexibility and reduce the emission of harmful pollutants, such as NO_x [1–3]. However, thermoacoustic instabilities, which result from a feedback loop of flame, flow, and acoustics, can occur in such systems [4].

The occurrence of thermoacoustic combustion instabilities has been thoroughly investigated and many recognized concepts regarding the mechanisms of interaction have already been identified, especially for low-frequency instabilities. There are several criteria to distinguish between low and high-frequency instabilities.

1. *Relation of instability frequency to flame cutoff.* Flames generally act like low-pass filters: velocity fluctuations above the flame cutoff frequency no longer lead to significant fluctuations in global heat release [5]. The dominant acoustic frequencies are typically well below this cutoff frequency for low-frequency instabilities. In contrast, no global flame response is observed at higher instability frequencies near or above the cutoff frequency, and heat release fluctuations may arise from direct interactions between the acoustic pressure and the flame [6,7].
2. *Non-compactness of the flame.* The Helmholtz number defines the compactness of a flame by relating the length of the flame δ_{fl} to the acoustic wavelength λ_a:

$$He = \frac{\delta_{\mathrm{fl}}}{\lambda_{\mathrm{a}}}. \tag{1}$$

   If this number exceeds a specific limit, the flame is considered non-compact, and local interaction mechanisms must be evaluated [7]. Global heat release rate fluctuations are no longer adequate to model thermoacoustic instabilities. Note that depending on flame length and operation conditions, instabilities in the range of a few kHz may still allow compact flames, which will be discussed in more detail in Section 5.
3. *Non-planar acoustics.* The propagation direction of the acoustics in high-frequency instabilities is not limited to the longitudinal direction but can also occur in the radial and transverse planes. This leads to the fact that the acoustic velocity can be perpendicular to the direction of flame propagation.

Due to its trajectory, the reacting transverse jet offers the special feature that no matter how the acoustics propagate in the combustion chamber (longitudinal, transverse, or radial), the acoustic velocity always acts orthogonally on the flame front in certain flame regions. This results in flame-flow-acoustic interaction mechanisms that have not been thoroughly investigated.

With this work, we want to show which interaction mechanisms can occur in the case of a self-excited thermoacoustic instability in the range of several thousand Hertz between flame, flow, and acoustics for a configuration with reacting jets in cross-flow and draw preliminary conclusions how these mechanisms can be circumvented. Two variants of the second stage are considered: a technically premixed (TP) system, where acoustic fluctuations can cause fuel inhomogeneities and experimental data are available for validation, and a perfectly premixed (PP) system, with the first stage remaining technically premixed. The simulations are denoted according to the premixing of the stages. TP-TP stands for technically premixed first and second stage, and TP-PP for technically premixed first and perfectly premixed second stage.

The paper is structured as follows: We first recall well-known interaction mechanisms for thermoacoustic instabilities and explain how the RJC can interact. We then present the factors influencing the fluctuating heat release rate in the two cases for the reacting jet and subsequently identify the active feedback loops between pressure and heat release rate.

2. Interaction mechanisms for thermoacoustic instabilities

Thermoacoustic instabilities arise from a coupling between acoustics and the heat release rate. These processes can be indirect, meaning that there is an intervening mechanism. Fig. 1 presents the response of the reacting jet in cross-flow to pressure disturbances at the flame.

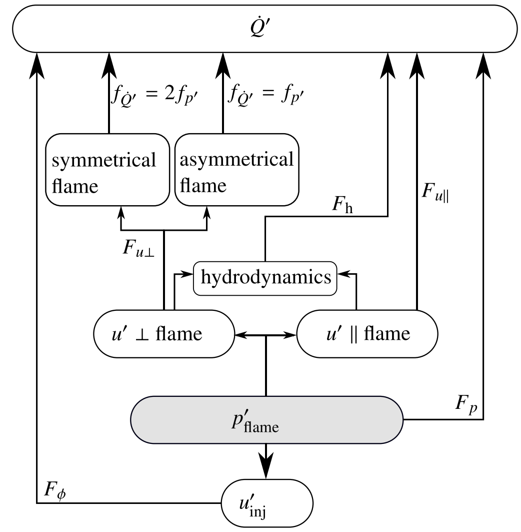

Fig. 1. Possible interaction paths from pressure fluctuations at the flame to heat release fluctuations. Effects which take place downstream (upstream) are positioned above (below) the element p'_{flame}.

2.1. Flame response to fuel inhomogeneities (F_ϕ)

In a technically premixed system, the thermoacoustic feedback loop can develop due to velocity fluctuations at the injector caused by pressure disturbances at the flame base. Fuel inhomogeneities developing near the injector are then convectively transported to the flame [8]. The term "injector coupling" was initially introduced to describe the interplay between transverse modes and fuel mass flow fluctuations in rocket engines' injectors [9]. This term was adopted for technically premixed concepts in gas turbines exposed to transverse modes [10]. We use this term when any pressure disturbance, regardless of direction, causes velocity fluctuations in the tube of the unburnt fuel.

To the authors' best knowledge, there are no studies on the behavior of non-premixed jets in cross-flow exposed to acoustic disturbances at the flame root. Brouzet et al. [11] investigated a related configuration with a cross-flow velocity of $u_{\mathrm{c}} = 0$. Their work supports the hypothesis that transversal modes generate strong longitudinal fluctuations in the mixing tube that drive fuel inhomogeneities and shows that this mechanism has to be considered for this kind of system. Plascencia et al. [12] focused on the positioning of the jet in the acoustic field. They observed a different flame response, whether the flame was sitting in a pressure node or anti-node.

2.2. Flame response to parallel velocity disturbances ($F_{u\|}$)

Pressure fluctuations at the burner mouth can trigger velocity disturbances parallel to the flame propagation direction. The acoustic velocity at the flame base causes a convective *displacement* followed by a *restoration* process of the flame surface [13,14], which lead to fluctuations in the heat release [15–18]. In several studies, Ånestad et al. [19,20] investigated a burner with a perfectly premixed reacting jet in cross-flow. They showed that the air split ratio of the first and second stage could be a controlling parameter for instability [19]. A simple time delay model with $\tau = L_{\mathrm{fl}}/u_{\mathrm{flow}}$ explained the instability, where L_{fl} is the characteristic flame length and u_{flow} is the bulk velocity. Adjusting the time delay of the first stage by reducing the speed proved to be significantly more effective than adjusting τ_2 of the second stage, which brought the heat release rates of the two flame regions out of phase [20].

2.3. Flame response to orthogonal velocity disturbances ($F_{u\perp}$)

2.3.1. Symmetrical flame

Only in the limiting case $u_c = 0$, the symmetric flame occurs. Sharifi et al. [21] observed that the flame reacts directly to the acoustic velocity with compression (pressure node) and displacement (pressure anti-node). However, O'Connor et al. [10] considered this effect to be small. Similar conclusions were reported by Urbano and Selle [22] in the context of rocket engines, and by Acharya et al. [23] for swirl flames. Purwar et al. [24] made another discovery: the heat release of symmetrical flames reacts at twice the frequency to transversal velocity fluctuations. The flame reacts similarly to a disturbance from the left and the right [25], breaking the feedback between pressure and heat release modulations.

2.3.2. Asymmetrical flame

Choi et al. [26,27] investigated the behavior of a reacting jet in cross-flow to orthogonal velocity fluctuations under self-excited [26] and forced [27] conditions. The position of the jet proved to have an effect on amplification for thermoacoustic instabilities. When placed in the pressure node, the jet showed a flapping motion due to acoustic velocity fluctuations and responded with delayed global heat release [26]. They could also demonstrate that besides the flapping motion of the jet, harmonic mass flux ejections were a dominating source of heat release fluctuations [27], being an indication that an injector coupling effect was present.

2.4. Flame response to hydrodynamics (F_h)

According to Hemchandra et al. [28], the flow field can influence the thermoacoustic feedback loop by amplifying acoustic perturbations or developing self-excited instabilities that drive the thermoacoustic instability through flame heat release modulations. O'Connor [29] demonstrated that coupling with hydrodynamics can have a decisive influence on heat release for several flame configurations, predominantly including low-frequency cases. The reacting jet in cross-flow offers a variety of vortex structures [30]. Bonnaire and Polifke [31] showed that manipulating the shear layer using elliptical jets can trigger combustion instabilities of different frequencies. The cross-flow's natural shear layer activity at high frequencies could amplify thermoacoustic instabilities by synchronizing the acoustic and hydrodynamic frequencies. Omi et al. [32] showed that tuning the momentum flux ratio of jet to cross-flow adjusted the frequency in the pressure scalogram until it lead to thermoacoustic instabilities. Chakravarthy et al. [33] showed in a backward-facing step combustor that, for a cold-flow configuration, increasing the flow velocity often caused the dominant frequency to lock onto the acoustic cavity frequencies. In contrast, for a reacting flow, the dominant frequency alternated between two vortex-shedding modes [34].

2.5. Direct flame response to pressure modulations (F_p)

The direct mechanism describes that the chemical reaction rate and the density of unburned gases depend on pressure [6]. Sharifi et al. [21, 35] showed that the density variation due to compression contributes significantly to the source term of thermoacoustic instability.

3. Test cases

The geometry investigated is based on an experiment conducted at the German Aerospace Center (DLR). The high-pressure test rig HBK-S, known from previous work, for example, by Lammel et al. [36] and Fiolitakis et al. [37], was equipped with a second stage realized by a reaction jet in cross-flow on three of the six side walls of the hexagonal combustion chamber. For the case of technical premixing, time-averaged OH* chemiluminescence line-of-sight (LOS) images of the first stage and a pressure spectrum are presented in Section 6. The configurations and the dimensions used in this study are shown in Fig. 2. A single burner of the second stage provides close to 6% of the total power, while a burner of the first stage produces approximately 7% of the total power. The fuel mass flux is 0.0166 kg/s, which translates into a total power of approximately 1 MW. Detailed operating conditions for the first and the second stage are listed in Tables 1 and 2. The experiments were performed at an absolute pressure of 7 bar.

Table 1
Boundary conditions for the TP-TP simulation.

	1st stage (TP)	2nd stage (TP)
Fuel comp. [vol − %]	60 H_2 - 40 CH_4	60 H_2 - 40 CH_4
Air comp. [v −%]	79 N_2 - 21 O_2	79 N_2 - 21 O_2
$\dot{m}_{fuel}$ [kg s^{-1}]	0.0138	0.0028
$\dot{m}_{air}$ [kg s^{-1}]	0.5203	0.1066
T_{fuel} [K]	333.15	333.15
T_{air} [K]	673.15	673.15
u_j [m s^{-1}]	110	90
ϕ [−]	0.53	0.53
Outlet pressure [bar]	7	

Table 2
Boundary conditions for the TP-PP simulation. The first stage remains unchanged compared to the TP-TP simulation. Hence, the details for the first stage are listed in Table 1.

	2nd stage (PP)
Fuel comp. [vol − %]	60 H_2 - 40 CH_4
Air comp. [vol − %]	79 N_2 - 21 O_2
$\dot{m}_{fuel\ line}$ [kg s^{-1}]	0.0028
$\dot{m}_{air\ line}$ [kg s^{-1}]	0.1066
$T_{fuel\ line}$ [K]	636.5
$T_{air\ line}$ [K]	636.5
u_j [m s^{-1}]	90
ϕ [−]	0.53
Mixture fraction	0.0258
Outlet pressure [bar]	7

4. Numerical model

Large eddy simulation using the Siemens PLM software Star-CCM+ version 18.06 is applied [38]. The turbulent dynamic viscosity is calculated using the WALE model [39]. The chemical reactions are solved using the flamelet-generated manifolds introduced by Bradley and Lau [40] and advanced by van Oijen and de Goey [41], using 1D premixed strained flamelets realized by an opposed flow (fresh-to-burnt) configuration, based on the San Diego detailed mechanism. Only CO and CO_2 are considered for calculating the progress variable, which is a suitable fit for most hydrocarbon fuels [38]. We know the limitations of the unity Lewis number assumption that this approach includes. The overestimated thermal diffusivity weakens the effects of preferential diffusion, reducing differences in local flame speed and, in extreme cases, potentially leading to thermodiffusive instabilities. Work by Shi et al. [42,43] suggests that these effects are less relevant when increasing turbulence. For validation, we compare averaged (Fig. 6) and frequency-filtered line-of-sight images (Fig. 13) and pressure spectra (Fig. 5), which will be discussed later. These comparisons demonstrate that the simulation corresponds well with experiments despite neglecting the effects of non-unity Lewis-number treatment.

The turbulent-chemistry interaction on subgrid scales is represented using a thickened flame model, originally introduced by Colin et al. [44], dynamically adjusted following the idea of Legier et al. [45]. The flame sensor is based on the progress variable and the power-law model by Charlette et al. [46] is applied for the efficiency function. The flame is resolved with eight grid cells in the reaction zone. The

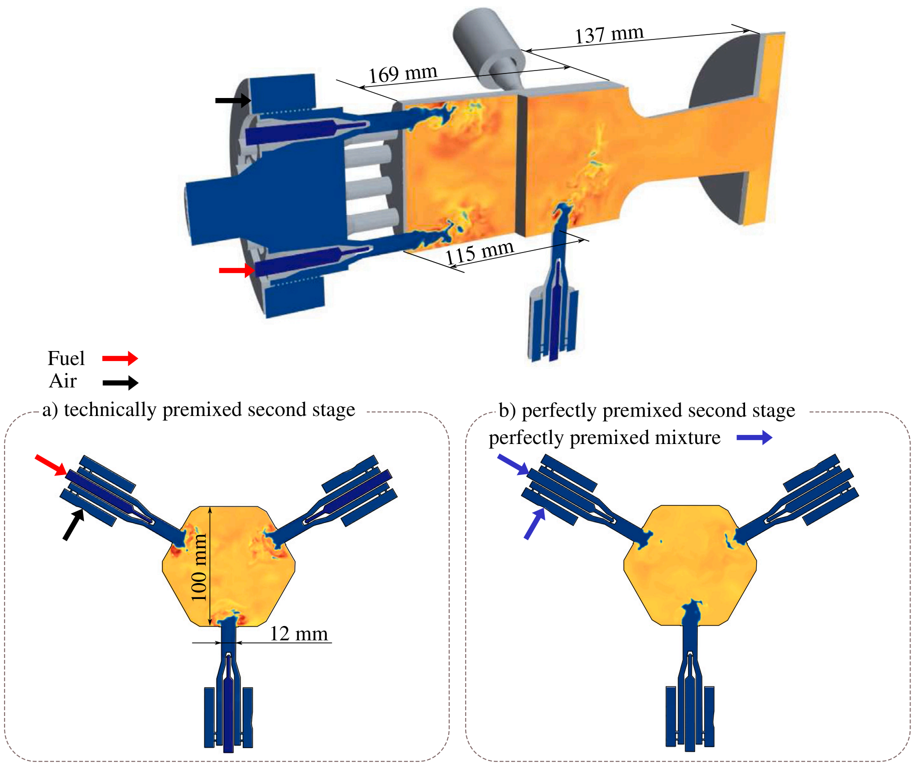

Fig. 2. Geometry and flow structure of the investigated configuration.

thickening factors are $F = 20 - 30$, and the efficiency function corrects for the lack of flame wrinkling on resolved scales. Although conventional practice is to use the model for moderate thickening factors, of $F = 5 - 10$ (see recent works from Detomaso et al. [47] and Agostinelli et al. [48]), smaller thickenings would be disproportionately computationally expensive for the 15 very thin high-pressure hydrogen flames in this combustion chamber. Under these conditions, the chosen approach appears reasonable, as the simulation consistently reproduces the essential physical trends.

The outlet is extended by a 450 mm long cylinder (not shown in Fig. 2). This strategy avoids a strong interaction of the acoustics with the numerical boundary condition, and a pressure boundary condition with $p' = 0$ is chosen at the outlet. The inlet boundary conditions are specified as mass flows, without additional acoustic boundary conditions. Since the perforated plates are included in the simulation, the system can be considered acoustically closed at these locations. The walls are modeled as adiabatic because no precise wall temperatures were available in the experiment. This assumption leads to a slight overestimation of the mode frequency, which is considered acceptable.

The base mesh, shown in Fig. 3, consists of 12.6 million polyhedral cells. Detailed information on cell sizes can be found in Table 3. To investigate the inherent convergence of the filtered quantities, the mesh was refined by a factor of 0.8 and coarsened by a factor of 1.2 (simulation TP-TP), resulting in 18.4 million cells for the fine mesh and 9.8 million cells for the coarse mesh.

Analysis of the power spectra of turbulent kinetic energy at sample points in the combustion chamber and mixing tube, and the integrated heat release, show a similar spectral energy decay for all three grids (Fig. 4). The fine mesh shows slightly lower turbulent kinetic energy. Further analysis also revealed attenuated pressure fluctuations for the unstable first longitudinal mode. In contrast, higher-frequency (>5000 Hz) modes are more pronounced (not shown) which are not apparent in the experiment. The base mesh guarantees at least 50 cells per wavelength for the modes investigated, and the acoustic CFL number is around 1.5 in the hot regions around the flame. Based on

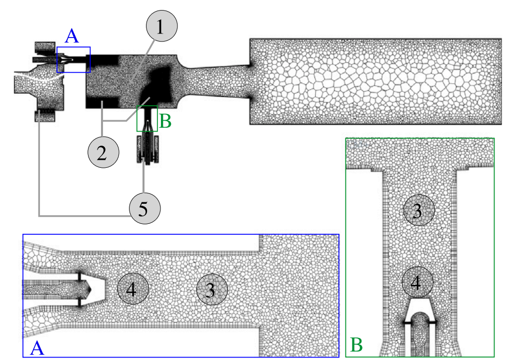

Fig. 3. Slice of the computational base-mesh with a detailed view showing the injectors. The circled numbers indicate the areas quantified in Table 3 by their characteristic cell size.

these results, the base mesh is considered sufficient as it best balances computational effort and reliability. For a simulation duration of 100 ms, the computational demand is approximately 50000 CPU hours.

Both simulations start with initial conditions based on a RANS simulation. Then, the PISO scheme, which is only of first order in time discretization in StarCCM+, is used for 140 ms applying a time step of 5 μs, aiming for damping acoustic waves originating from the drasitical impulse by switching from RANS to LES. Then, the time integration method is changed to a second-order implicit scheme using a time step of 1 μs. This procedure, already shown by Ho et al. [49], proved to be an efficient way of initializing LES simulations for conditions that are not subject to acoustic waves as a result of numerical artifacts.

Table 3
Information about the cell count and cell size of the computational base-mesh. The circled numbers indicate the areas listed in Fig. 3. Numbers are scaled by 0.8 for the finer mesh and 1.2 for the coarser mesh, yielding 18.4 and 9.8 million cells, respectively.

	Value	Unit
Number of cells	12,648,178	–
① Combustion chamber	2	mm
② Flame region	0.45	mm
③ Premixing duct (coarse)	0.5	mm
④ Premixing duct (fine)	0.375	mm
⑤ Perforated plate	0.75	mm
Number of Prism Layers	3	–

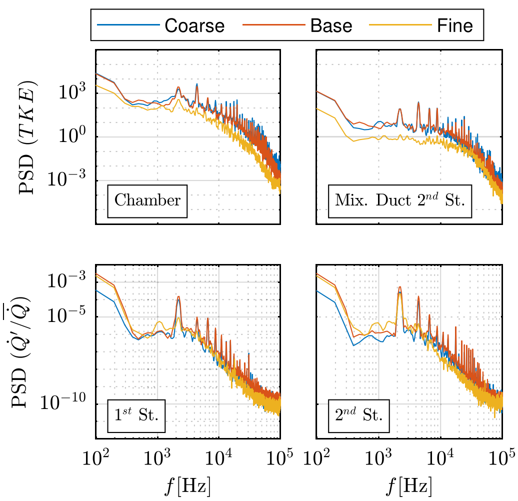

Fig. 4. Power spectral density of the resolved turbulent kinetic energy and the integrated heat release for the technically premixed axial stage at the location indicated in the lower left of each figure.

5. Analysis framework

In the next sections, we will describe our observations of the thermoacoustic limit cycle and propose possibilities for mitigating the unstable behavior.

Fundamentally, the stability behavior of a system can be described using the balance equation for the disturbance energy:

$$\frac{\partial E}{\partial t} + \nabla \cdot \boldsymbol{I} = D, \tag{2}$$

where E is the disturbance energy density, $\boldsymbol{I}$ is the flux, and D contains the sources and sinks. If the sources are stronger than the sinks and the flux of acoustic energy across the boundaries, the disturbance energy increases [50]. Nonlinear effects cause the rate of change of the disturbance energy to vanish, and the system enters a limit cycle.

If the acoustic energy is chosen as the norm for the disturbance energy, and the flow is assumed to be irrotational, non-diffusive in momentum and energy, homentropic, without mean flow, in chemical equilibrium, and subject to only small perturbations, the classical Rayleigh source term is obtained [51]:

$$\frac{\partial}{\partial t}\left(\frac{1}{2}\bar{\rho}u_i'u_i' + \frac{1}{2}\bar{\rho}c^2\left(\frac{p'}{\gamma\bar{p}}\right)^2\right) + \nabla\cdot(p'\boldsymbol{u}') = \frac{\gamma-1}{\gamma\bar{p}}p'\dot{q}', \tag{3}$$

where ρ is the density, u_i the velocity components, c the speed of sound, γ the ratio of specific heats, p the pressure and $\dot{q}$ the volumetric heat release. Quantities denoted by $\bar{()}$ indicate the mean state and $()'$ the fluctuation defined as $()' = () - \bar{()}$. The thermoacoustic source term, in this form known as the Rayleigh index RI yields

$$RI = \int_V p'\dot{q}'\mathrm{d}V, \tag{4}$$

where V is the combustor volume. $RI > 0$ is a necessary but not sufficient criterion for thermoacoustic instabilities and we interpret RI as the strength of the thermoacoustic driving.

The flames of the first and second stage can be considered compact given the flame length (see Figs. 6 and 8) and the mode structure (see Fig. 9). Consequently, we only consider integrated heat release and no local interaction of pressure and heat release. The comparison of the local and integral Rayleigh terms is shown for the two configurations in Figs. 12 and 17 and shows very good agreement for all flames, except for the second stage in the TP-TP simulation. We explain the deviation by the fact that the pressure sample was taken at the cross-sectional transition to the combustion chamber, where the pressure is already slightly lower than inside the combustion chamber.

The integrated heat release $\dot{Q}$ along a flame surface A is a function of the unburnt density ρ_u, the enthalpy of the reaction h_r, and the flame speed s_l:

$$\dot{Q} = \int_{A_\mathrm{fl}} \rho_\mathrm{u} h_\mathrm{r} s_\mathrm{l} dA, \tag{5}$$

$$\dot{Q} = \rho_\mathrm{u} h_\mathrm{r,fl} s_\mathrm{l,fl} A_\mathrm{fl}, \tag{6}$$

where the subscript fl denotes the average of the respective quantity on the flame surface.

In a linearized framework, the following contributions to normalized fluctuations of heat release rate can be identified:

$$\frac{\dot{Q}'}{\bar{\dot{Q}}} = \frac{\rho_\mathrm{u}'}{\bar{\rho}_\mathrm{u}} + \frac{h_\mathrm{r,fl}'}{\bar{h}_\mathrm{r,fl}} + \frac{s_\mathrm{l,fl}'}{\bar{s}_\mathrm{l,fl}} + \frac{A_\mathrm{fl}'}{\bar{A}_\mathrm{fl}} \tag{7}$$

We will examine the quantities from Eq. (7) on an isosurface of the normalized progress variable $c = 0.5$ in frequency space and visualize the magnitude and argument of the Fourier coefficient (marked as $\hat{(\cdot)}$ in Fig. 14) at the unstable frequency with a pointer in the complex plane. This procedure allows us to draw conclusions about which interactions influence the global heat release and thus lead to a positive Rayleigh criterion. Note that the unburnt density ρ_u is evaluated in the mixing tube and not on the isosurface. The perturbations of the enthalpy of reactions $h_\mathrm{r,fl}'$ are expressed as fluctuations of equivalence ratio ϕ' as they are directly measurable. The laminar flame speed is calculated based on the correlation of Gülder [52], choosing the parameters for methane as fuel. The area A is evaluated as the total surface of the isosurface $c = 0.5$. We know Eq. (7) is a massive simplification, given that we are not investigating a laminar flame, but rather a turbulent flame using the thickened flame model. Nevertheless, we limit ourselves to a straightforward approach in this analysis, without daring to incorporate turbulence's influence, for example, through the efficiency function, since all variables in Eq. (7) are evident from the simulation and can be interpreted easily. Further approaches to correct the laminar flame speed based on the turbulent consumption and displacement velocity in acoustically excited turbulent flames were presented, for example, by Hemchandra et al. [53].

The data is processed at selected 2D planes using dynamic mode decomposition (DMD), introduced by Peter Schmid [54], to visualize the flame's dynamics. The data is then converted back to the time domain using only the zero-frequency and first strongest non-zero-frequency mode using

$$\boldsymbol{x}(t) = \sum_{k=1}^{r} \boldsymbol{\psi}_k e^{\omega_k t} b_k, \tag{8}$$

where $\boldsymbol{\psi}_k$ represents the modes and ω_k is a complex frequency. b_k is the initial condition of mode k and r is the number of modes taken into consideration. This procedure represents an effective method for filtering noise and highlighting the dynamics at the unstable frequency. Detailed information on the DMD routine used in this study can be found in [31].

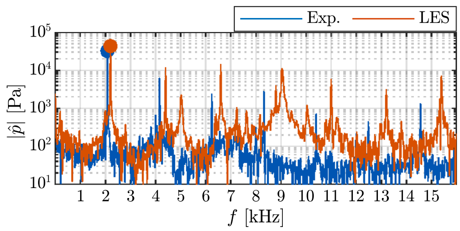

Fig. 5. Experimental and numerical pressure spectra for the TP-TP case exhibit peaks at 2090 Hz (32 200 Pa) and 2188 Hz (43 200 Pa), respectively.

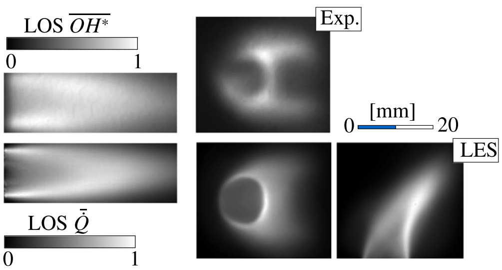

Fig. 6. Line-of-sight recording of the time-averaged OH* chemiluminescence from the experiment (upper row) is compared with the line-of-sight integration of the mean heat release rate from the simulation for the TP-TP case. Left: First stage, middle: top view on second stage, right: side view on second stage.

6. Thermoacoustic spectrum and mean flame shape

Figs. 5 and 7 show the pressure spectra for the two cases. The technically premixed case settles into a 1L mode at 2188 Hz with an amplitude of 43 200 Pa, which is in very good agreement with experimental findings. The experimental counterpart shows the mode at 2090 Hz with a slightly lower amplitude of 32 200 Pa. The probe location is approximately 40 mm upstream of the second stage.

Mean flame shapes are compared in Fig. 6. We note that OH* is not a suitable indicator for accurately representing heat release in technically premixed simulations [55,56]. Hence, it is used only for qualitative comparison.

The first stage flame is reproduced very well in terms of shape and length. In the second stage, the flames exhibit similar characteristic lengths but differ slightly immediately downstream in the top view, where the LES predicts a more uniform heat release. It should be emphasized that these results represent averages of a highly dynamic process, as can be seen later in Fig. 13. In addition, we present LES results showing a side view of the axial stage, where the characteristic curved shape of the transverse jet becomes apparent.

We also refer to the Supplementary Material, which presents another case in which the 1L mode was not observed experimentally due to an extended mixing section of the first stage; this absence is correctly predicted by the simulation.

The perfectly premixed case settles in a mixed longitudinal-transversal mode at 5027 Hz. No experimental data are available for this case. The pressure amplitude is slightly higher at 75 000 Pa compared to the TP-TP case. It should be noted that the pressure probe was positioned downstream of the second stage. If the same location as in the TP-TP simulation were chosen, it would be located in a pressure node. The averaged LOS images show no significant changes in the first stage. However, in the second stage, a more homogeneous pattern downstream can be seen in the top view. Furthermore, a slightly greater penetration depth is visible in the side view compared to the TP-TP case.

Mode shapes are illustrated in Fig. 9.

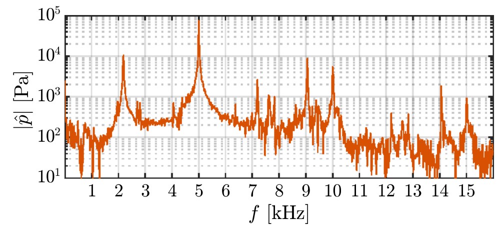

Fig. 7. Numerical pressure spectra for the TP-PP case exhibit a peak at 5027 Hz (75 000 Pa).

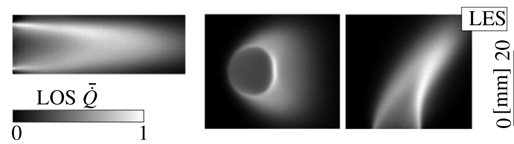

Fig. 8. Line-of-sight integration of the mean heat release rate from the TP-PP simulation. Left: First stage, middle: top view on second stage, right: side view on second stage.

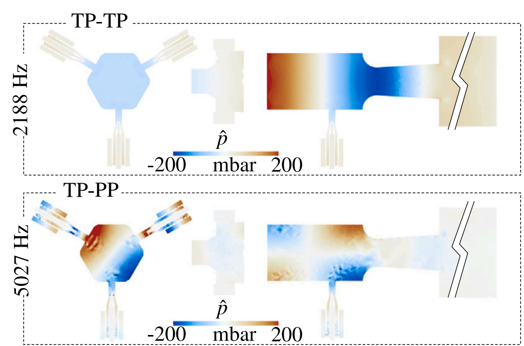

Fig. 9. Surface Fast Fourier Transform of the two cases. The simulation with technically premixed second stage shows a standing longitudinal mode (top), the simulation with perfectly premixed second stage exhibits a rotating longitudinal-transversal mixed mode (bottom).

7. Technically premixed second stage

Fig. 10 shows pressure series close to the injector, surface-averaged equivalence ratio at the dump plane, and volume-integrated heat release of a single first and second stage flame, respectively. We observe fluctuations of p, ϕ at the dump plane and $\dot{Q}$ at 2188 Hz. Importantly, fuel inhomogeneities are not dissipated completely while they are transported by convection from the injector to the flame. Interestingly, heat release perturbations are much more significant in the second stage, even though the equivalence ratio fluctuations are minor compared to the first stage. This leads to the conclusion that another mechanism, in addition to equivalence ratio fluctuations, must drive the flame's heat release perturbations in the second stage.

Fig. 11 shows in-phase pressure and heat release fluctuations for a single flame of first and second stage, which indicates that $RI > 0$ in both the first and second stage. Pressure values are directly taken in the mixing tube at the axial position of the dump plane. Fig. 12 shows the Rayleigh index for all flames, calculated locally and with integrated heat release. All flames exhibit similar driving potential. In the second stage, the deviation is attributed to a lower pressure signal at the reference position.

First stage. Fig. 13 shows a reconstruction of the distribution of the heat release rate on a cut plane by the DMD routine explained in Section 5. The images are all sorted so that the maximum heat release always occurs at $\theta = 90°$.

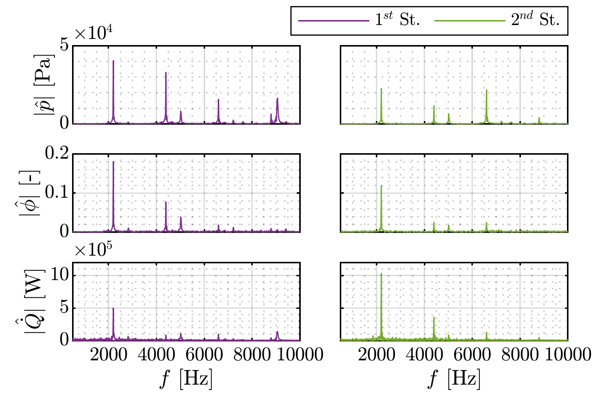

Fig. 10. Spectra of pressure, equivalence ratio and integrated heat release for first stage (left) and second stage (right) of the TP-TP simulation.

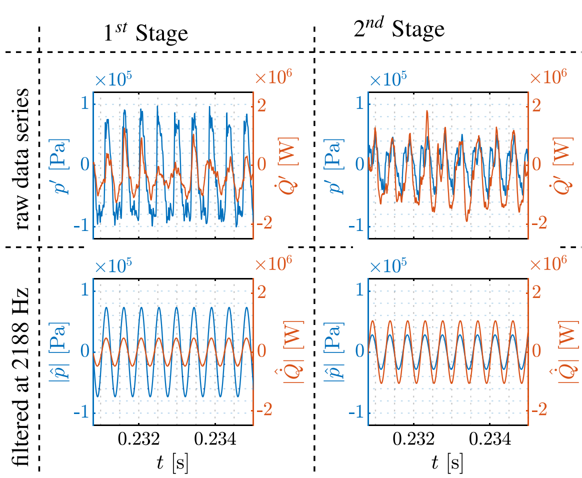

Fig. 11. Fluctuating pressure at the downstream end of the mixing tube and integrated heat release of the associated flame for the TP-TP case.

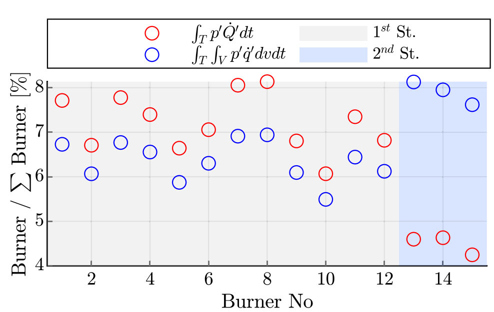

Fig. 12. Comparison of the local and integrated Rayleigh indices for all burners for the TP-TP case, where the contribution of the individual burners is related to the Rayleigh index of the entire combustion chamber. Deviations in the second stage arise from a reduced pressure signal at the reference location.

The flame spreads radially at the instant of maximum heat release. Subsequently, significant heat release occurs near the burner mouth. After that, we see signs of flame pinch-off; heat release is low, and the flame is short.

Fig. 14 depicts individual contributions shown in Eq. (7) in frequency space as phasor plots. Laminar flame speed is significant. Since we are dealing with highly turbulent combustion, laminar flame speed can only serve as an indicator. Additionally, isentropic compression of the unburnt gases increases their temperature, also leading to higher flame speeds [57,58]. For the first stage, we see a dominant influence of the equivalence ratio. As already mentioned by Cho and Lieuwen [59] and Albayrak et al. [60], the equivalence ratio directly influences the laminar flame speed, the effect of which we cannot quantify here.

Second stage. The reconstructed plots of the heat release by the DMD routine reveals a severely disturbed flame front (Fig. 13). The flame root gets tilted upstream (LES Slice, Side view), which is the strongest when the cross-flow velocity has the most substantial fluctuation in the upstream direction (minimum in axial velocity fluctuation) between $\theta = 135°$ and $\theta = 180°$. This perturbation destroys flame surface. The flame then restores and the heat release at its maximum at $\theta = 90°$. The line-of-sight images show a ring-shaped pattern upstream, which is created when the flame is deflected in this direction and is more pronounced in the LES compared to the experiment. When bending back in the flow direction, the flame anchors itself more clearly at the burner mouth in the experiment. At the same time, the simulation shows less heat release in the region around the burner exit.

This leads to the conclusion that acoustically induced velocity perturbation that generate and annihilate flame surface is a powerful feedback mechanism.

For the second stage the phasor diagram confirms that flame surface modulations significantly impact the heat release rate (see Fig. 14). The modulations of the flame surface of the second stage are much more intense than in the first stage, and they are in phase with the heat release. We also observe equivalence ratio and flame speed modulations in phase.

These findings highlight the need for a transfer function in further studies that quantitatively links orthogonal velocity fluctuations to heat release for the reacting jet in cross-flow, enabling the stability behavior to be assessed with established acoustic solvers utilizing a flame model. In this context, the hypothesis of Choi and Kim [26] that multiple axially distributed stages can disrupt acoustic-flame coupling appears consistent, as phase relations between pressure and velocity change across every pressure node and antinode in a standing wave. As a result, the phase relation between pressure and heat release changes accordingly.

8. Perfectly premixed simulation

Fig. 15 shows pressure, equivalence ratio, and heat release perturbation for the PP simulation. As described above, we see a longitudinal-transversal mixed mode at 5072 Hz in absence of equivalence ratio perturbation in the second stage. However, we see comparable amount of heat release perturbations in the first and second stage.

We also see that heat release and pressure are in phase from Fig. 16. The Rayleigh index in Fig. 17 shows comparable driving potential for all burners. Likewise, no difference is discernible between the local and compact descriptions.

First stage. We see minor periodic wrinkling of the flame in the reconstructed heat release plots (Fig. 18). Flame length stays relatively constant.

The phasor plot in Fig. 14 shows equivalence ratio-driven heat release fluctuations. However, weaker fluctuations, as observed at the dump plane, reach the flame. The wrinkling of the flame leads to fluctuations in the flame surface, that are not in phase with the heat release. Flame speed and density fluctuations are dominant drivers for the heat release fluctuations.

Second stage. Fig. 18 shows vortex activity in the flame's shear layer for the second stage. As shown in our previous study [31], the hydrodynamic frequency of the reacting jet couples with the acoustic frequency. One may expect the resulting flame surface modulations to be in phase with the acoustic pressure. However, this is not the case, as Fig. 14 shows.

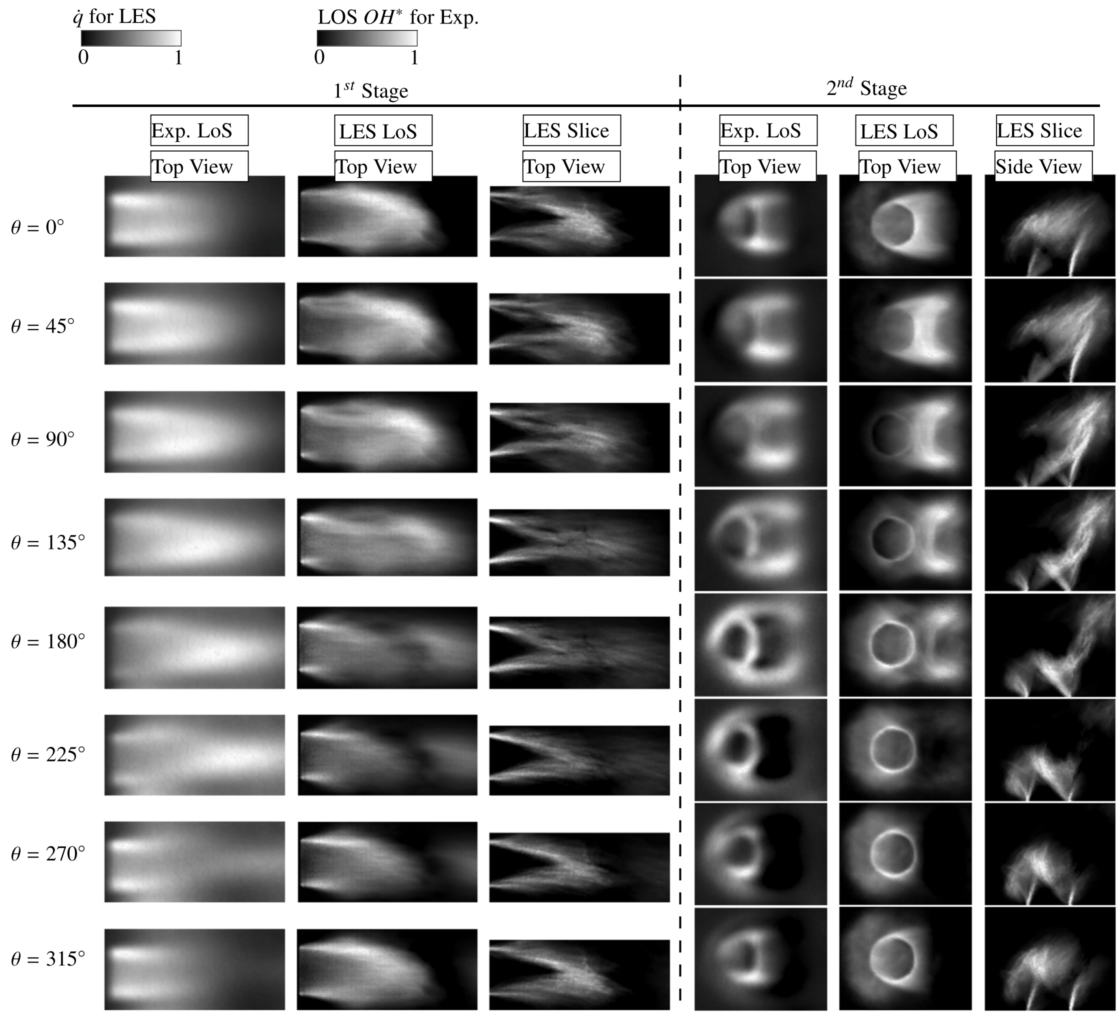

Fig. 13. Reconstructed flame images for the TP–TP case were obtained from the dominant DMD modes and normalized by their respective maxima. The images show the highest OH*/heat release at $\theta = 90°$.

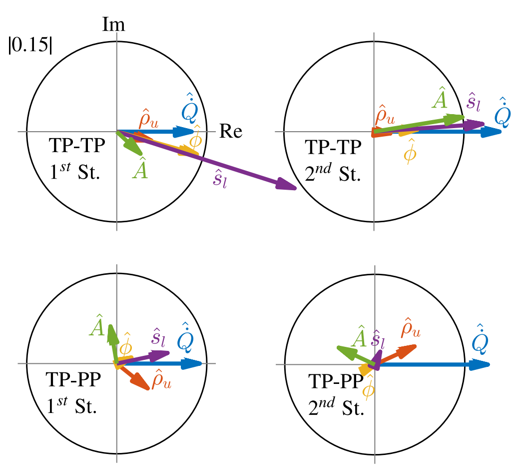

Fig. 14. Phasor plots of the quantities shown in Eq. (7) at the unstable frequency (2188 Hz for TP-TP and 5027 Hz for TP-PP) at one selected flame for the first and second stage.

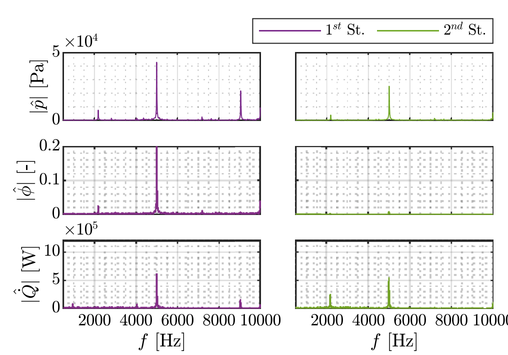

Fig. 15. Pressure, equivalence ratio and heat release perturbation for the TP-PP simulation.

This suggests that flame surface modulations, resulting from the periodic vortex shedding of the reacting jet in cross-flow, are not an important element of the thermoacoustic feedback in the present case (see Fig. 14). Thus, we cannot quantify the contribution of this strong shear layer activity to the flame response. Only density fluctuations are in phase with heat release fluctuations. The mode, visualized in Fig. 9, is a rotating mode and, thus, has a dynamic node line in the cross-sectional area. Consequently every flame of the second stage is exposed to a fluctuating pressure maximum. The density fluctuations originating from isentropic compression are the leading mechanism for the transversal mode acting on the perfectly premixed flame. In addition, the pressure is highest at the combustion chamber wall, where

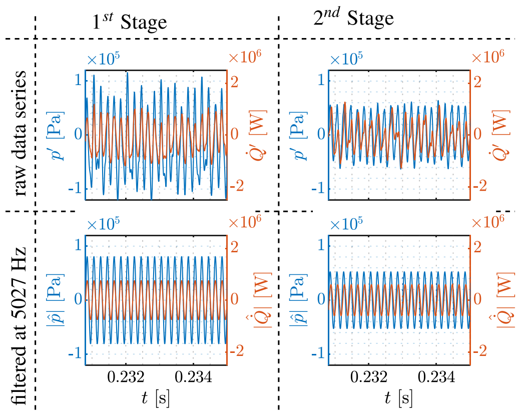

Fig. 16. Fluctuating pressure at the downstream end of the mixing tube and integrated heat release of the associated flame for the TP-PP case.

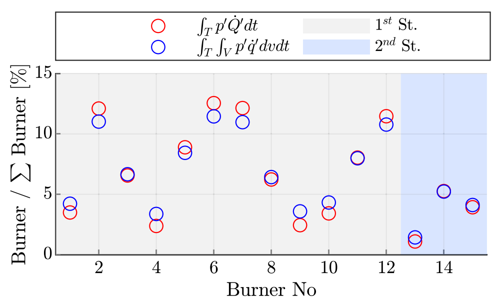

Fig. 17. Comparison of the local and integrated Rayleigh indices for all burners for the TP-PP case, where the contribution of the individual burners is related to the Rayleigh index of the entire combustion chamber.

the reacting jet releases heat. Thus, this mechanism is stronger in the second stage than in the first stage. Due to the longitudinal component of the mode, axial relocation to regions of lower acoustic pressure remains a possible mitigation strategy in this configuration. Sharifi et al. [35] also investigated the contribution of individual components of the flame surface density model to heat release. Forced simulations showed that the influence of density has the most significant impact in a configuration where the flame is located in the pressure antinode consistent with the results in the present study.

9. Conclusion

This paper presents interaction mechanisms of the thermoacoustic feedback loop in an industrially relevant, high-pressure, two-stage combustor for a reacting jet in cross-flow with hydrogen addition, offering insights into preliminary approaches to mitigation strategies. Differentiating between a technically premixed and a perfectly premixed reacting jet in cross-flow offers possibilities of specifically separating pathways from pressure fluctuations to heat release perturbations. We observe a mode switch between these two setups, highlighting the need for operation-point-specific thermoacoustic tuning. The compact flame assumption remains valid for the unstable modes in both cases. Therefore, conclusions are drawn based on the interaction between pressure fluctuations and integral heat release. For the technically premixed second stage, the strong flame response to the orthogonal velocity fluctuation shows that the asymmetric flame of the reacting jet in cross-flow responds at the same frequency, unlike what Zellhuber et al. [25] and Purwar et al. [24] demonstrated for the symmetric flame. Relocating the second stage should mitigate this mechanism.

The phasor plots show a strong coupling between equivalence ratio fluctuations and heat release, suggesting that manipulating the mixing

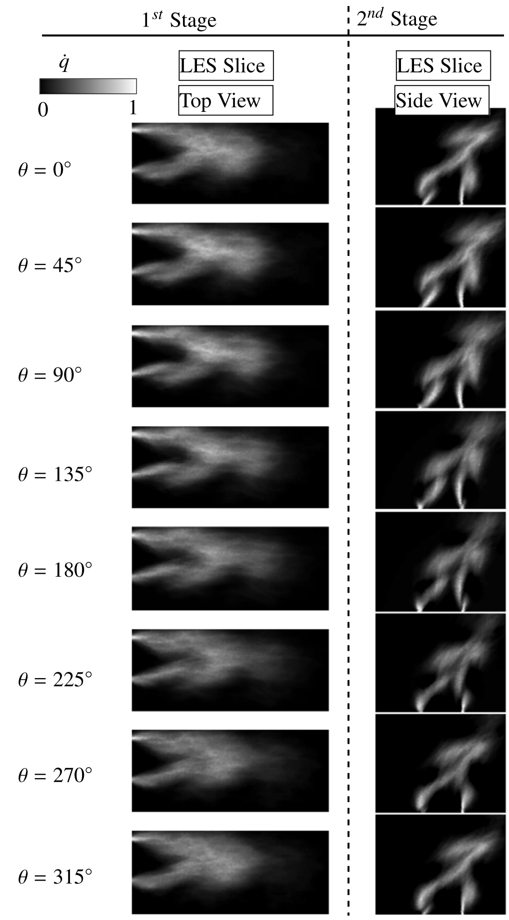

Fig. 18. Reconstructed flame images for the TP–PP case were obtained from the dominant DMD modes and normalized by their respective maxima. The images show the highest heat release at $\theta = 90°$.

length and thus influencing the time delay is a practical lever for preventing positive feedback.

The coupling of the shear layer activity of the jet with the acoustic frequency, as shown in the case of [31], proves to be a robust subject of thermoacoustic instability in the perfectly premixed simulation. The strong influence of the direct mechanism of pressure fluctuation on heat release fluctuation, as already demonstrated by Sharifi et al. [21] for the jet flame, makes it challenging to derive damping strategies for this mechanism in the reacting jet in cross-flow.

CRediT authorship contribution statement

Philip Bonnaire: Writing – review & editing, Writing – original draft, Visualization, Validation, Software, Project administration, Methodology, Formal analysis, Conceptualization. **Sven Romeikat:** Writing – review & editing, Investigation. **Lukasz Panek:** Writing – review & editing, Methodology, Conceptualization. **Oliver Lammel:** Writing – review & editing, Methodology, Investigation, Data curation. **Jonas Eigemann:** Writing – review & editing, Methodology, Conceptualization. **Andreas Kempf:** Writing – review & editing, Methodology, Conceptualization. **Wolfgang Polifke:** Writing – review & editing, Supervision, Methodology, Conceptualization.

Declaration of competing interest

The authors declare that they have no known competing financial interests or personal relationships that could have appeared to influence the work reported in this paper.

Acknowledgments

The research initiative “InnoTurbinE AP 1.3” was funded by the Federal Ministry for Economic Affairs and Energy and Siemens Energy Global GmbH & Co. KG as part of an AG Turbo project under the grant agreement number 03EE5041F, whose financial support is deeply appreciated. Funding for the experiments was provided under the AG Turbo project “LaBreVer AP 1.1” (grant no. 0324295B). The authors gratefully acknowledge the computational and data resources provided by the Leibniz Supercomputing Centre.

Appendix A. Supplementary data

Supplementary Material related to this article represents an additional case study with longer mixing section length of the first stage.

Supplementary material related to this article can be found online at https://doi.org/10.1016/j.combustflame.2025.114549.

References

[1] M.R. Bothien, A. Ciani, J.P. Wood, G. Fruechtel, Toward decarbonized power generation with gas turbines by using sequential combustion for burning hydrogen, J. Eng. Gas Turbines Power 141 (2019) 121013.
[2] M. Otero, T. Genova, B. Stiehl, A.J. Morales, S. Martin, K.A. Ahmed, The influence of pressure on flame-flow characteristics of a reacting jet in crossflow, J. Energy Resour. Technol. 144 (2022) 052301.
[3] B. Stiehl, M. Otero, T. Genova, T. Worbington, J. Reyes, S. Martin, C. Velez, K. Ahmed, Simulation of premixed and partially premixed jet-in-crossflow flames at high pressure, J. Eng. Gas Turbines Power 143 (2021) 031001.
[4] T. Poinsot, Prediction and control of combustion instabilities in real engines, Proc. Combust. Inst. 36 (2017) 1–28.
[5] E. Æsøy, T. Indlekofer, F. Gant, A. Cuquel, M.R. Bothien, J.R. Dawson, The effect of hydrogen enrichment, flame-flame interaction, confinement, and asymmetry on the acoustic response of a model can combustor, Combust. Flame 242 (2022) 112176.
[6] Y. Méry, Dynamical response of a perfectly premixed flame and limit behavior for high power density systems, Combust. Flame 192 (2018) 410–425.
[7] T. Hummel, F. Berger, M. Hertweck, B. Schuermans, T. Sattelmayer, High-frequency thermoacoustic modulation mechanisms in swirl-stabilized gas turbine combustors—part II: Modeling and analysis, J. Eng. Gas Turbines Power 139 (2017) 071502.
[8] T. Lieuwen, B.T. Zinn, The role of equivalence ratio oscillations in driving combustion instabilities in low nox gas turbines, Symp. (Int.) Combust. 27 (1998) 1809–1816.
[9] S. Gröning, J. Hardi, D. Suslov, M. Oschwald, Injector-driven combustion instabilities in a hydrogen/oxygen rocket combustor, J. Propuls. Power 32 (2016) 560–573.
[10] J. O’Connor, V. Acharya, T. Lieuwen, Transverse combustion instabilities: Acoustic, fluid mechanic, and flame processes, Prog. Energy Combust. Sci. 49 (2015) 1–39.
[11] D. Brouzet, S. You, M.A. Plascencia, M. Roa, M. Ihme, The dynamics of non-premixed flames subjected to a transverse acoustic mode, Combust. Flame 246 (2022) 112330.
[12] M.A. Plascencia, M. Roa, A.R. Karagozian, D.G. Talley, Turbulent nonpremixed jet flames under transverse acoustic forcing, in: AIAA Propulsion and Energy 2020 Forum, American Institute of Aeronautics and Astronautics, 2020, VIRTUAL EVENT.
[13] R.S. Blumenthal, P. Subramanian, R. Sujith, W. Polifke, Novel perspectives on the dynamics of premixed flames, Combust. Flame 160 (7) (2013) 1215–1224.
[14] D.-H. Shin, T. Lieuwen, Flame wrinkle destruction processes in harmonically forced, laminar premixed flames, Combust. Flame 159 (11) (2012) 3312–3322.
[15] W. Polifke, Combustion instabilities, in: J. Anthoine, A. Hirschberg (Eds.), Advances in Aeroacoustics and Applications, in: VKI LS 2004-05, Von Karman Institute, 2004.
[16] C.J. Lawn, W. Polifke, A model for the thermoacoustic response of a premixed swirl burner, part II: The flame response, Combust. Sci. Technol. 176 (2004) 1359–1390.
[17] T. Schuller, D. Durox, S. Candel, A unified model for the prediction of laminar flame transfer functions: Comparisons between conical and V-Flame dynamics, Combust. Flame 134 (2003) 21–34.
[18] A. Huber, W. Polifke, Dynamics of practical premix flames, part II: identification and interpretation of CFD data, Int. J. Spray Combust. Dyn. 1 (2009) 229–249.
[19] A. Ånestad, R. Sampath, J. Moeck, A. Gruber, N.A. Worth, The structure and stability of premixed CH4, H2, and NH3/H2 Flames in an axially staged can combustor, J. Eng. Gas Turbines Power 146 (2024) 051002.
[20] A. Ånestad, E. Æsøy, J.R. Dawson, N.A. Worth, Mitigating thermoacoustic instabilities in premixed hydrogen flames using axial staging, Proc. Combust. Inst. 40 (2024) 105430.
[21] V. Sharifi, A.M. Kempf, C. Beck, Large-eddy simulation of acoustic flame response to high-frequency transverse excitations, AIAA J. 57 (2019) 1–14.
[22] A. Urbano, L. Selle, Driving and damping mechanisms for transverse combustion instabilities in liquid rocket engines, J. Fluid Mech. 820 (2017) R2.
[23] V. Acharya, Shreekrishna, D.-H. Shin, T. Lieuwen, Swirl effects on harmonically excited, premixed flame kinematics, Combust. Flame 159 (2012) 1139–1150.
[24] N. Purwar, M. Haeringer, B. Schuermans, W. Polifke, Flame response to transverse velocity excitation leading to frequency doubling and modal coupling, Combust. Flame 230 (2021) 111412.
[25] M. Zellhuber, L. Tay-Wo-Chong, W. Polifke, Non-linear flame response at small perturbation amplitudes – Consequences for analysis of thermoacoustic instabilities, in: Proceedings of the European Combustion Meeting, 2011.
[26] Y. Choi, K.T. Kim, Mode shape-dependent thermoacoustic interactions between a lean-premixed primary flame and an axially-staged transverse reacting jet, Combust. Flame 255 (2023) 112884.
[27] Y. Choi, G. Han, K.-T. Kim, Forced response of transverse reacting jet in vitiated crossflow to harmonic velocity disturbances, Combust. Flame 269 (2024) 113670.
[28] S. Hemchandra, S. Shanbhogue, S. Hong, A.F. Ghoniem, Role of hydrodynamic shear layer stability in driving combustion instability in a premixed propane/air backward facing step combustor, Phys. Rev. Fluids (2018) 063201.
[29] J. O’Connor, Understanding the role of flow dynamics in thermoacoustic combustion instability, Proc. Combust. Inst. 39 (2022) 4583–4610.
[30] T. Fric, A. Roshko, Vortical structure in the wake of a transverse jet, J. Fluid Mech. 279 (1994) 1–47.
[31] P. Bonnaire, W. Polifke, Analysis of high-frequency dynamics of a reacting jet in crossflow based on large eddy simulation, J. Eng. Gas Turbines Power 146 (2024) 031002.
[32] K. Omi, K. Nakayama, K. Hirose, K. Takizawa, H. Taguchi, S. Nakaya, M. Tsue, Nonlinear mode decomposition of combustion instabilities under various jet-to-crossflow momentum ratios in a hydrogen-rich ram combustor using a deep Koopman network, Combust. Flame 268 (2024) 113643.
[33] S. Chakravarthy, R. Sivakumar, O. Shreenivasan, Vortex-acoustic lock-on in bluff-body and backward-facing step combustors, Sadhana 32 (2007) 145–154.
[34] S.R. Chakravarthy, O.J. Shreenivasan, B. Boehm, A. Dreizler, J. Janicka, Experimental characterization of onset of acoustic instability in a nonpremixed half-dump combustor, J. Acoust. Soc. Am. 122 (2007) 120–127.
[35] V. Sharifi, C. Beck, B. Janus, A.M. Kempf, Design and testing of a high frequency thermoacoustic combustion experiment, AIAA J. 59 (2021) 1–17.
[36] O. Lammel, H. Schütz, G. Schmitz, R. Lückerath, M. Stöhr, B. Noll, M. Aigner, M. Hase, W. Krebs, FLOX® combustion at high power density and high flame temperatures, J. Eng. Gas Turbines Power 132 (2010) 121503.
[37] A. Fiolitakis, M. Pries, O. Lammel, T. Kathrotia, Investigation of high-frequency thermoacoustic instabilities in a FLOX® burner using large-eddy simulation and multi resolution proper orthogonal decomposition, in: AIAA SCITECH 2024 Forum, American Institute of Aeronautics and Astronautics, 2024.
[38] Siemens Industries Digital Software, Simcenter STAR-CCM+, 2023.
[39] F. Nicoud, F. Ducros, Subgrid-scale stress modelling based on the square of the velocity gradient tensor, Flow Turbul. Combust. 62 (1999) 183–200.
[40] D. Bradley, A.K.C. Lau, The mathematical modelling of premixed turbulent combustion, Pure Appl. Chem. 62 (1990) 803–814.
[41] J.A. van Oijen, L.P.H. de Goey, Modelling of premixed laminar flames using flamelet-generated manifolds, Combust. Sci. Technol. 161 (2000) 113–137.
[42] S. Shi, R. Schultheis, R.S. Barlow, D. Geyer, A. Dreizler, T. Li, Assessing turbulence–flame interaction of thermo-diffusive lean premixed H2/Air flames towards distributed burning regime, Combust. Flame 269 (2024) 113699.
[43] S. Shi, R. Schultheis, R.S. Barlow, D. Geyer, A. Dreizler, T. Li, Internal flame structures of thermo-diffusive lean premixed H2/Air flames with increasing turbulence, Proc. Combust. Inst. 40 (1–4) (2024) 105225.
[44] O. Colin, F. Ducros, D. Veynante, T. Poinsot, A thickenend flame model for large eddy simulation of turbulent premixed combustion, Phys. Fluids 12 (2000) 1843–1863.
[45] J.P. Legier, T. Poinsot, D. Veynante, Dynamically thickened flame LES model for premixed and non-premixed turbulent combustion, 2000, Proceedings of the Summer Program.
[46] F. Charlette, C. Meneveau, D. Veynante, A power-law flame wrinkling model for les of premixed turbulent combustion part I: non-dynamic formulation and initial tests, Combust. Flame 131 (2002) 159–180.
[47] N. Detomaso, J.-J. Hok, O. Dounia, D. Laera, T. Poinsot, A generalization of the thickened flame model for stretched flames, Combust. Flame 258 (2023) 113080.

[48] P.W. Agostinelli, D. Laera, I. Chterev, I. Boxx, L. Gicquel, T. Poinsot, Large Eddy simulations of mean pressure and H 2 addition effects on the stabilization and dynamics of a partially-premixed swirled-stabilized methane flame, Combust. Flame 249 (2023) 112592.

[49] J.Z. Ho, S. Jella, M. Talei, G. Bourque, T. Indlekofer, J. Dawson, Assessment of the LES-FGM framework for capturing stable and unstable modes in a hydrogen / methane fuelled premixed combustor, Combust. Flame 255 (2023) 112904.

[50] B. Schuermans, J. Moeck, A. Blondé, B. Dharmaputra, N. Noiray, The Rayleigh integral is always positive in steadily operated combustors, Proc. Combust. Inst. 39 (4) (2022) 4661–4669.

[51] M.J. Brear, F. Nicoud, M. Talei, A. Giauque, E.R. Hawkes, Disturbance energy transport and sound production in gaseous combustion, J. Fluid Mech. 707 (2012) 53–73.

[52] Ö.L. Gülder, Correlations of laminar combustion data for alternative S.I. engine fuels, in: West Coast International Meeting and Exposition, 1984, 841000.

[53] S. Hemchandra, N. Peters, T. Lieuwen, Heat release response of acoustically forced turbulent premixed flames–role of kinematic restoration, Proc. Combust. Inst. 33 (1) (2011) 1609–1617.

[54] P.J. Schmid, Dynamic mode decomposition of numerical and experimental data, J. Fluid Mech. 656 (2010) 5–28.

[55] L.C. Haber, U. Vandsburger, W.R. Saunders, V.K. Khanna, An examination of the relationship between chemiluminescent light emissions and heat release rate under non-adiabatic conditions, in: ASME Turbo Expo 2000: Power for Land, Sea, and Air, in: Coal, Biomass and Alternative Fuels; Combustion and Fuels; Oil and Gas Applications; Cycle Innovations, vol. 2, ASME, Munich, Germany, 2000, V002T02A041.

[56] M. Lauer, T. Sattelmayer, On the adequacy of chemiluminescence as a measure for heat release in turbulent flames with mixture gradients, J. Eng. Gas Turbines Power 132 (6) (2010) 061502.

[57] M. Zellhuber, B. Schuermans, W. Polifke, Impact of acoustic pressure on auto-ignition and heat release, 1, Combust. Theory Model. 18 (2014) 1–31.

[58] J. Eigemann, P. Bonnaire, L. Panek, C. Beck, W. Polifke, A. Kempf, Amplification of thermoacoustic flame response to investigate high frequency combustion instabilities with LES, Combust. Flame 280 (2025) 114317.

[59] J.H. Cho, T.C. Lieuwen, Laminar premixed flame response to equivalence ratio oscillations, Combust. Flame 140 (1–2) (2005) 116–129.

[60] A. Albayrak, R.S. Blumenthal, A. Ulhaq, W. Polifke, An analytical model for the impulse response of laminar premixed flames to equivalence ratio perturbations, Proc. Combust. Inst. 36 (3) (2017) 3725–3732.